Chinese Journal of Chemical Engineering 89 (2026) 293–301

Contents lists available at ScienceDirect

Chinese Journal of Chemical Engineering

journal homepage: www.elsevier.com/locate/CJChE

Full Length Article

Multiphysics coupling rule of semi-coke catalytic tar cracking

Jie Feng [1, 2], Jun Xue [1], Yaowei Hu [1, 2], Yuncai Song [1, 2, *], Wenying Li [1, 2, *]

[1] State Key Laboratory of Clean and Efficient Coal Utilization, Taiyuan University of Technology, Taiyuan 030024, China
[2] Shanxi Research Institute of Huairou Laboratory, Taiyuan 030032, China

ARTICLE INFO

Article history:
Received 10 May 2025
Received in revised form
21 July 2025
Accepted 27 July 2025
Available online 8 January 2026

Keywords:
Catalysis
Semi-coke porosity structure
Toluene
Heat transfer
Mass transfer

ABSTRACT

This study investigates catalytic tar cracking over semi-coke catalysts, addressing reaction kinetics challenges by integrating experimental data with a COMSOL Multiphysics model. A multi-physics framework combines catalysis, carbon deposition, and self-consumption to analyze toluene (tar model compound) removal. The model evaluates intrinsic catalytic activity, porosity evolution, and porous media flow, revealing that toluene conversion is governed by diffusion/convective mass transfer, homogeneous reactions, and surface reactions influenced by dynamic carbon deposition/removal. Increasing temperature from 973 to 1173 K enhances gas-film heat and mass transfer coefficient, accelerating tar cracking rates and extending catalyst lifetime. Elevated temperatures improve gas-solid phase heat/mass transfer, promoting efficient tar removal during syngas purification. The results highlight the interplay between reaction kinetics, carbon deposition dynamics, and transport phenomena in optimizing semi-coke catalyst performance under high-temperature conditions.
© 2026 The Chemical Industry and Engineering Society of China, and Chemical Industry Press Co., Ltd. All rights are reserved, including those for text and data mining, AI training, and similar technologies.

1. Introduction

Semi-coke catalysts demonstrate cost-effectiveness and wide availability, serving as viable feedstocks for reactor applications even after deactivation [1]. Their utilization not only circumvents regeneration costs but also enables their repurposing as carbonaceous materials, offering distinct advantages for purifying gasification syngas with high tar content under demanding operational conditions [2–4]. However, these catalysts exhibit limited catalytic activity and are prone to rapid deactivation because they are gradually consumed through gasification reactions with steam and carbon dioxide present in the crude syngas [5–10]. Concurrently, carbon deposition from catalytic cracking and gasification-induced structural modifications alter the internal pore architecture of semi-coke [3,11], significantly influencing gas component diffusion within catalyst pores. The interdependent mechanisms of catalytic tar cracking, carbon substrate consumption, activity suppression through carbon deposition, and participation in steam/carbon dioxide reactions create complex synergistic effects [12]. These multi-physics interactions between chemical reactions, mass transfer, and structural evolution present substantial challenges in modeling semi-coke behavior within tar removal reaction system.

In preliminary investigations [13], kinetic modeling of catalytic tar cracking using biomass-derived char catalysts incorporated two critical parameters: catalyst activity coefficients and structural performance metrics. This approach systematically coupled catalytic activation mechanisms with deactivation kinetics. In studying catalyst deactivation mechanisms during methane reforming processes, Muradov *et al.* [14] employed Voorhies' empirical correlation [15] ($C_c = 0.52\theta^{0.38}$, where C_c denotes carbon deposition mass per catalyst particle) to quantify temporal evolution of coking phenomena on reforming catalysts. The interdependence between coking phenomena and reforming kinetics was mathematically formalized through an exponentially decaying activity correlation: $AF = \exp(Kt)$, where the activity factor (AF) quantifies residual catalytic capacity, K denotes the deactivation rate constant, and t characterizes the cumulative particle-gas interfacial exposure duration. This mathematical formulation establishes *a* direct correlation between catalytic activity and temporal exposure duration. However, while the investigation addressed temporal variations in catalyst performance within reactor systems, it neglected spatial heterogeneity across catalyst beds. Consequently, the model lacks critical data regarding radial activity gradients within the reactor's geometric configuration. Notably, the unique structural characteristics of semi-coke

* Corresponding authors.
E-mail addresses: songyuncai@tyut.edu.cn (Y. Song), ying@tyut.edu.cn (W. Li).

https://doi.org/10.1016/j.cjche.2025.07.016
1004-9541/© 2026 The Chemical Industry and Engineering Society of China, and Chemical Industry Press Co., Ltd. All rights are reserved, including those for text and data mining, AI training, and similar technologies.

particles introduce additional complexity-their highly developed pore networks govern gas transport dynamics through Knudsen diffusion mechanisms and providing reactive surface areas orders of magnitude greater than external geometric surfaces, fundamentally altering reaction-diffusion equilibria. The morphological parameters of porous networks must be rigorously accounted for their governing role in reaction kinetics, particularly through their dual modulation of reactant transport phenomena and active surface availability that fundamentally controls reaction-diffusion coupling mechanisms. Although pore architecture critically governs reaction dynamics in semi-coke catalysts, existing mechanistic models [7,14–19] simulating tar cracking and catalyst gasification have predominantly focused on carbon-deposition-induced deactivation mechanisms during thermal cracking processes, while neglecting structural evolution effects. Nevertheless, these models exhibit critical omissions by failing to incorporate char-phase reactivity dynamics and gasification-coupled deactivation mechanisms during catalytic processes. This conceptual gap underscores the pressing need to establish coupled models that resolve tripartite interactions among char gasification kinetics, coking phenomena, and catalytic cycles within multicomponent syngas environments.

To resolve the paradoxical behavior of semi-coke catalysts functioning simultaneously as reactive agents and consumable substrates, this study establishes a multiphysics coupling framework through COMSOL Multiphysics simulations. The model integrates three synergistic mechanisms: thermochemical interactions reconcile competing energy demands between endothermic tar cracking and exothermic gasification reactions, while structural dynamics capture time-dependent pore evolution governing Knudsen diffusion limitations. Concurrently, activity modulation algorithms resolve spatiotemporal deactivation patterns arising from the dynamic equilibrium between carbon deposition and substrate gasification. Focused investigations reveal three critical process interdependencies: (i) temperature-programmed deactivation pathways in syngas reactors exhibit strong nonlinear correlations with feedstock thermal profiles; (ii) particle-level analyses identify porosity-dependent reaction-diffusion bottlenecks governing mid-life catalyst performance; and (iii) mechanistic studies demonstrate that carbon-based catalyst deposition accelerated the catalyst deactivation. This integrated approach not only enables precise prediction of consumable catalyst lifetimes but also establishes universal scaling laws applicable to heterogeneous reaction systems experiencing concurrent catalytic activation and structural degradation.

2. Experimental

2.1. Description of semi-coke catalytic cracking reactor

In this study, an online syngas purification system was developed for *in situ* removal of deactivated catalysts in a 10000 $m^3 \cdot h^{-1}$ gasification reactor [20]. A gas-solid countercurrent moving-bed reactor configuration was employed for tar catalytic cracking using semi-coke catalysts. Fresh semi-coke catalyst particles are continuously fed from the reactor top, through which raw syngas flows upward undergoing tar decomposition. Spent catalyst particles are discharged from the reactor bottom into the gasifier, where they serve as gasification feedstock, thereby eliminating regeneration costs while enhancing carbon utilization efficiency. The integrated reactor design and process schematic are detailed in Fig. 1. The geometric model parameters of the tar cracking reactor are as follows: The diameter is 8.54 cm, the filling height of the catalyst is 25.12 cm, the inclination Angle of the bottom cone area is 62.5°, the bottom diameter of the bottom cone is 4 cm, and the height is 2 cm.

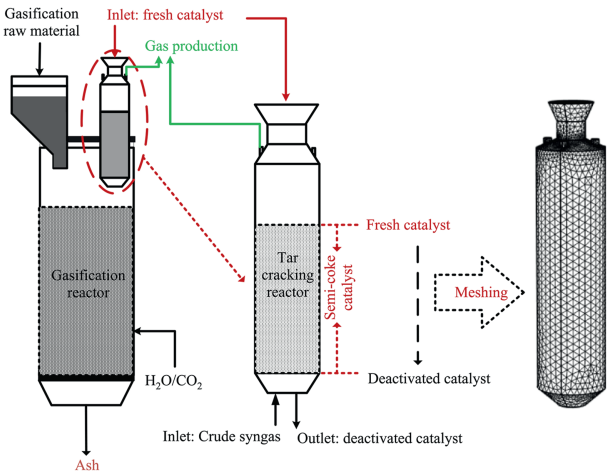

Fig. 1. Reactor configuration and mesh division.

The reactor is equipped with a total of 4 outlets, with a diameter of 1 cm at each outlet. The radius of the top silo is 3 cm, the radius of the bottom is 2 cm, and the height is 2 cm.

2.2. Key assumptions of the model

A computational model was formulated in this study to investigate the key mechanisms governing tar catalytic cracking using semi-coke catalysts. The model framework incorporates four fundamental assumptions:

(1) Semi-coke particles are modeled as homogeneous spherical entities with uniform physicochemical properties and monodisperse size distribution, maintaining structural integrity throughout reaction cycles;
(2) Continuum-scale gas flow through the porous medium maintains momentum conservation, with interconnected pores explicitly resolved while closed porosity is neglected;
(3) The gaseous phase behaves as a weakly compressible flow governed by the ideal gas law;
(4) Adiabatic boundary conditions are imposed on reactor walls, excluding external thermal interactions.

2.3. Muti-field coupling of the model

Based on the conservation equations of momentum, mass, and energy, this study establishes the multiphysics field characteristics within the semi-coke catalytic tar cracking reactor. The dynamic behavior of tar cracking in raw syngas was systematically investigated through a theoretical framework integrating three transport phenomena (momentum, mass, energy) with chemical reactions. Fig. 2 schematically illustrates the coupled transport-reaction mechanisms governing this gas-solid system.

2.3.1. Governing equations for momentum, mass and heat transfer

The conservation equations governing mass, momentum, and heat transfer across reactor-scale and particle-scale domains are systematically presented in Table 1 (mass balance), Table 2 (momentum conservation), and Table 3 (heat transfer equation).

2.3.2. Kinetics of chemical reactions

The reactions involved in the catalytic cracking of tar by semi-coke and their kinetic data are shown in Table 4 and Table 5.

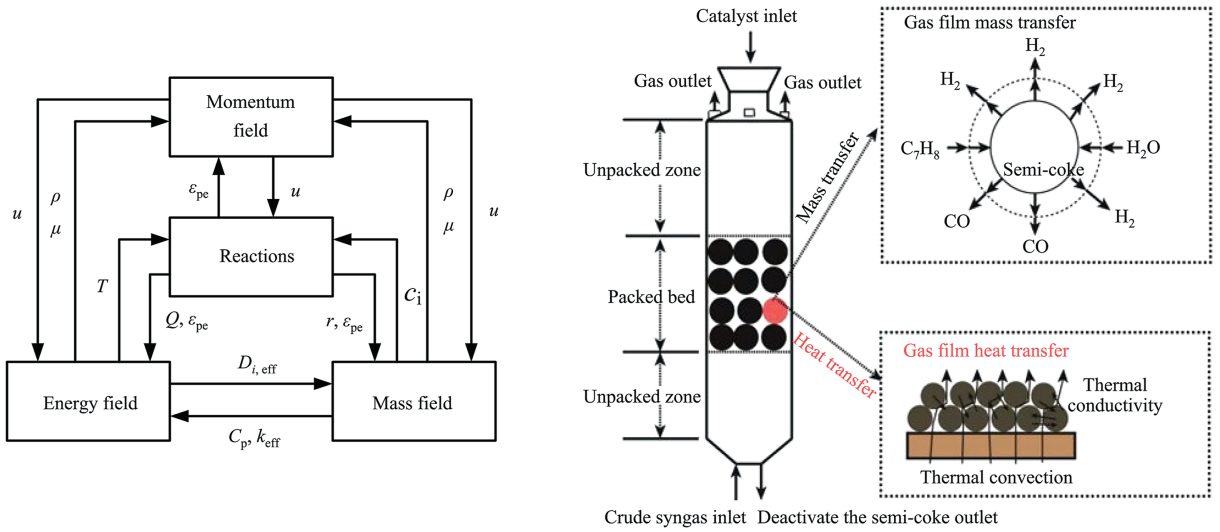

Fig. 2. Multiphysics coupling mechanism integrating three transport phenomena (mass, energy, momentum) and chemical reactions, highlighting gas-solid interfacial transport dynamics within the reactor.

Table 1
Mass transfer within systems at multiple scales [21–23].

Type of equation	Equation	No.
Mass transfer equation	$\varepsilon_p\rho\frac{\delta w_i}{\delta t}+\nabla j_i+\rho(u\cdot\nabla)w_i=R_i$	(1)
Gas film mass transfer	$j_i=\sum_i\left(h_{D,i}\left(c_i-c_{pe,i}\right)\right)_{r=1}$	(2)
Gas film mass transfer coefficient	$h_{D,i}=\frac{ShD}{r_{pe}}$	(3)
Sherwood number	$Sh=2+0.522Re^{1/2}Sc^{1/3}$	(4)
Reynolds number	$Re=\frac{d_{pe}u\rho}{\mu}$	(5)
Schmidt number	$Sc_i=\frac{\nu}{D_i}$	(6)
Particle internal mass transfer equation	$\varepsilon_p\rho\frac{\delta w_{pe,i}}{\delta t}+\frac{1}{r^2r_{pe}^2}\frac{\delta(r^2j_i)}{\delta r}+\frac{1}{r_{pe}}\rho u_r\frac{\delta w_{pe,i}}{\delta r}=R_{pe,i}+S_{pe,reac}R_{pe,i}$	(7)
Particle surface area	$S_{pe,reac}=\frac{6(1-\varepsilon_{pe})}{d_{pe}}$	(8)
Pore diffusion in particles	$D_{i,eff}^{mk}=\frac{1}{e^2}\left(\frac{1}{D_i^m+D_i^k}\right)^{-1}$ $D_{i,eff}^{k}=\frac{2r}{3}\sqrt{\frac{8RT}{pM_i}}$	(9)

Table 2
The momentum field solves the velocity model.

Type of equation	Equation	NO.
Momentum equation for the empty bed region	$\rho\frac{\delta u}{\delta t}+\rho(u\cdot\nabla)u=\nabla[-pI+K]+F$	(10)
Bed gap momentum equation	$\frac{1}{\varepsilon_p}\rho\frac{\delta u}{\delta t}+\frac{1}{\varepsilon_p}\rho(u\cdot\nabla)u\frac{1}{\varepsilon_p}=\nabla[-pI+K]-\left(\mu\kappa^{-1}+\beta\rho\lvert u\rvert+\frac{Q_m}{\varepsilon_{pe}^2}\right)u+F$	(11)
The viscous stress term	$\kappa=\mu\frac{1}{\varepsilon_p}(\nabla u+(\nabla u)^T)-\frac{2}{3}\mu\frac{1}{\varepsilon_p}(\nabla\cdot u)I$	(12)
Gas-solid mass exchange	$\frac{\delta\varepsilon_{pe}\rho}{\delta t}+\nabla\cdot(\rho u)=Q_m$	(13)

2.3.3. Catalyst activity and pore change equation

By incorporating the modified random pore model (RPM) [29,30], the change in particle porosity was linked to the carbon substrate conversion rate (x), as shown in Eq. (22), Eqs. (23) and (24). Among them, k_{RPM} is the reaction rate constant of the random well model, and $k_{RPM}=A_0\exp(-E_0/RT)$. A_0 is pre-exponential factor and E_0 are active energy.

$$\frac{dx}{dt}=k_{RPM}(1-x)\sqrt{1-\psi\ln(1-x)} \tag{22}$$

$$\psi=\frac{4\pi L_0(1-\varepsilon_{pe})}{S_{pe}^2} \tag{23}$$

Table 3
Heat transfer equation in multiscale system [22,24].

Type of equation	Equation	No.
Energy conservation equations within the bed	$\varepsilon_p\rho_f c_{p,f}\frac{\delta T}{\delta t}+\rho_f c_{p,f}u\cdot\nabla T_f+\nabla\cdot q_f=Q_{pe,f}+\varepsilon_p Q_f$	(14)
The air film transfers heat	$Q_{pe,f}=-S_{pe}h_{pe,f}(T_f-T_{pe})$	(15)
Gas film heat transfer coefficient	$h_{pe,f}=\left[d_{pe}\left(\frac{1}{k_f Nu}+\frac{1}{10k_{pe,eff}}\right)\right]^{-1}$	(16)
Energy conservation equations within particles	$(\rho c_p)_{pe,eff}\frac{\delta T_{pe}}{\delta t}+\frac{1}{r^2 r_{pe}^2}\frac{\delta\left(-r^2 k_{pe,eff}\frac{\delta T_{pe}}{\delta r}\right)}{\delta r}=Q_{pe}$	(17)
Effective specific heat capacity of particles	$(\rho c_p)_{pe,eff}=\varepsilon_{pe}\rho_f c_{p,f}+(1-\varepsilon_{pe})\rho_{pe}c_{p,pe}$	(18)
Effective thermal conductivity of particles	$k_{pe,eff}=\varepsilon_{pe}k_f+(1-\varepsilon_{pe})k_{pe}$	(19)
Nusselt number	$Nu=(7-10\varepsilon_{pe}+5\varepsilon_{pe}^2)(1+0.7Re^{0.2}Pr^{1/3})+(1.33-2.4\varepsilon_{pe}+1.2\varepsilon_{pe}^2)Re^{0.7}Pr^{1/3}$	(20)
Prandtl number	$Pr=\frac{C_p\mu}{k}$	(21)

Table 4
The main reaction equation, enthalpy change and reaction rate expression in the system [19,25–28].

Equation of reaction	ΔH/kJ·mol^{-1}	Reaction rate expression
$C_7H_8\rightarrow 7C+4H_2$	−50.0	$r_1=1.03\times10^{13}\exp\left(-\frac{324500}{RT}\right)C_{C_7H_8}$
$CH_4\rightarrow C+2H_2$	74.6	$r_2=\frac{k_2K_{CH_4,2}\left(P_{CH_4}-\frac{P_{H_2}^2}{K_{P,2}}\right)}{\left(1+K_{CH_4,2}P_{CH_4}+\frac{P_{H_2}^{1.5}}{K_{H_2,2}}\right)}$
$C_7H_8+7H_2O\rightarrow 7CO+11H_2$	725.0	$r_3=\left(k_{3,f}\frac{C_{co}C_{H_2O}}{C_{H_2}^{0.5}}-k_{3,b}C_{CO}C_{H_2}^{0.5}\right)\Big/\mathrm{DEN}^2$
$CO_2+H_2\rightleftharpoons CO+H_2O$	41.2	$r_4=\frac{k_4K_{CO_2,4}K_{H_2,4}P_{CO_2}P_{H_2}}{(1+K_{CO_2,4}P_{CO_2}+K_{H_2,4}P_{H_2})^2}\left(1-\frac{P_{CO}P_{H_2O}}{K_{P,4}P_{H_2}P_{CO_2}}\right)$
$CO_2+C\rightarrow 2CO$	+172.4	$r_5=\frac{\frac{k_5}{K_{CO_2,5}K_{CO,5}}\left(\frac{P_{CO_2}}{P_{CO}}-\frac{P_{CO}}{K_{P,5}}\right)}{\left(1+K_{CO,5}P_{CO}+\frac{1}{K_{CO_2,5}K_{CO,5}}\frac{P_{CO_2}}{P_{CO}}\right)^2}$
$CH_4+H_2O\rightleftharpoons CO+3H_2$	205.9	$r_6=3.10\times10^3 e^{-\frac{124700}{RT}}C_{CH_4}C_{H_2O}$
$CH_4+CO_2\rightleftharpoons 2CO+2H_2$	247.0	$r_7=\frac{k_7K_{CO_2,7}K_{CH_4,7}P_{CH_4}P_{CO_2}}{(1+K_{CO_2,7}P_{CO_2}+K_{CH_4,7}P_{CH_4})^2}\left(1-\frac{(P_{CO}P_{H_2})^2}{K_{P,7}P_{CH_4}P_{CO_2}}\right)$
$C+H_2O\Leftrightarrow CO+3H_2$	131.3	$r_8=\frac{\frac{k_8}{K_{H_2O,8}}\left(\frac{P_{H_2O}}{P_{H_2}}-\frac{P_{CO}}{K_{P,8}}\right)}{\left(1+K_{CH_4,8}P_{CH_4}+\frac{1}{K_{H_2O,8}}\frac{P_{H_2O}}{P_{H_2}}+\frac{P_{H_2}^{1.5}}{K_{H_2,8}}\right)^2}$

$$\varepsilon_{pe}(x)=\varepsilon_{pe,t=0}+x\left(1-\varepsilon_{pe,t=0}\right) \quad (24)$$

The gasification decarburization and carbon deposition reactions together influence the pore changes in semi-coke particles, and the effective diffusion coefficient of gas components within the pore channels of the semi-coke particles is directly related to the particle porosity. The differential equation for the particle porosity (ε_{pe}) as a function of carbon content variation is given in Eq. (25) [31].

$$\frac{d\varepsilon_{pe}}{dt}=\frac{-\varepsilon_{pe}C_c^m M_c}{\rho_{soot}} \quad (25)$$

To investigate the correlation between catalytic activity α and carbon deposition, a deactivation model for catalyst activity with respect to coke deposition was incorporated, as shown in Eq. (25) [31].

$$\frac{da}{dt}=-k_a r^2 C_c a \quad (26)$$

2.3.4. Method of calculation

The main effective components involved in syngas production are H_2, CO, and CO_2, and the yields of these components were calculated using Eqs. (26)–(28):

$$\text{Hydrogen yield}: \quad Y_{H_2}=\frac{F_{H_2,out}}{18\times F_{C_7H_8,in}}\times 100\% \quad (27)$$

$$\text{Carbon monoxide yield}: Y_{CO}=\frac{F_{CO,out}}{7\times F_{C_7H_8,in}}\times 100\% \quad (28)$$

$$\text{Carbon dioxide}: \quad Y_{CO_2}=\frac{F_{CO_2,out}}{7\times F_{C_7H_8,in}}\times 100\% \quad (29)$$

2.3.5. Initial values and boundary conditions

In this study, raw syngas were derived from the gasification process of organic solid waste at the kilogram scale [27]. The raw

Table 5
Kinetic reaction rate parameter in reaction equation [19,25–28].

Parameters	Value	Parameters	Value
k_2	$6.95\times10^{3}\exp\left(-\frac{58893}{RT}\right)$	$K_{P,5}$	$1.9393\times10^{9}\exp\left(-\frac{168527}{RT}\right)$
$K_{CH_4,2}$	$0.21\exp\left(-\frac{567}{RT}\right)$	k_7	$1.29\times10^{6}\exp\left(-\frac{102065}{RT}\right)$
$K_{P,2}$	$2.98\times10^{5}\exp\left(-\frac{84400}{RT}\right)$	$K_{CO_2,7}$	$2.61\times10^{-2}\exp\left(-\frac{37641}{RT}\right)$
$K_{H_2,2}$	$5.18\times10^{7}\exp\left(-\frac{133210}{RT}\right)$	$K_{CH_4,7}$	$2.60\times10^{-2}\exp\left(-\frac{40684}{RT}\right)$
$k_{3,f}$	$99\exp\left(-\frac{100000}{RT}\right)\mathrm{mmol\cdot m^{-2}\cdot min^{-1}}$	$K_{P,7}$	$6.78\times10^{14}\exp\left(-\frac{259660}{RT}\right)$
$k_{3,b}$	$66\exp\left(-\frac{1.36\times10^{8}}{RT}\right)\mathrm{mmol\cdot m^{-2}\cdot min^{-1}}$	k_8	$5.5\times10^{9}\exp\left(-\frac{166397}{RT}\right)$
k_4	$0.35\times10^{6}\exp\left(-\frac{81030}{RT}\right)$	$K_{H_2O,8}$	$4.73\times10^{-6}\exp\left(-\frac{97770}{RT}\right)$
$K_{CO_2,4}$	$0.5771\exp\left(-\frac{9262}{RT}\right)$	$K_{CH_4,8}$	$3.49\exp\left(-\frac{0}{RT}\right)$
$K_{H_2,4}$	$1.494\exp\left(\frac{6025}{RT}\right)$	$K_{P,8}$	$1.3827\times10^{7}\exp\left(-\frac{125916}{RT}\right)$
$K_{P,4}$	$56.4971\exp\left(-\frac{36580}{RT}\right)$	$K_{H_2,8}$	$7.34\times10^{-6}\exp\left(-\frac{100395}{RT}\right)$
k_5	$1.34\times10^{15}\exp\left(-\frac{243835}{RT}\right)$	$K_{CO,5}$	$7.34\times10^{-6}\exp\left(-\frac{100395}{RT}\right)$
$K_{CO_2,5}$	$2.81\times10^{7}\exp\left(-\frac{104085}{RT}\right)$		

Note: $\mathrm{DEN}=1+K_{CO}P_{CO}+K_{H_2}P_{H_2}+K_{CH_4}P_{CH_4}+K_{H_2O}P_{H_2O}/P_{H_2}$

syngas had an inlet temperature of 1173.15 K, and the tar cracking process utilized the waste heat from the raw syngas. The flow rate of the raw syngas was 0.669 $m^3\cdot h^{-1}$, and the inlet pressure was 101.325 kPa. The composition of the raw syngas was represented by the molar fraction *x*. The physical parameters of the raw syngas mixture were calculated using the formula provided in Table 6, and the specific component distribution of the raw syngas is shown in Table 7.

Table 7
Composition distribution of crude syngas.

Name of substance	Mole fraction
H_2O	0.21
H_2	0.18
C_7H_8	2.4×10^{-3}
CO	0.21
CO_2	0.08
CH_4	0.18
N_2	0.1376

Table 6
Physical property parameters used in the model.

Physical property parameters	Numerical value or expression
Specific heat capacity	$C_{p,\mathrm{gas}}=\sum_i w_i\frac{C_{p,i}}{M_n};\ w_i=\frac{c_iM_i}{\sum_i c_iM_i};\ C_{p,\mathrm{gas}}=800\ \mathrm{J\cdot kg^{-1}\cdot K^{-1}}$
Specific heat ratio	$\gamma=\frac{C_p}{C_p-R_g}$
Thermal conductivity	$k_{\mathrm{gas}}=0.5\left(\sum_i x_ik_i+\frac{1}{\sum_i\frac{x_i}{k_i}}\right)$
	$x_i=\frac{c_i}{\sum_i c_i};\ k_{\mathrm{cat}}=1.68\ \mathrm{W\cdot m^{-1}\cdot K}$
Density	$\rho_{\mathrm{gas}}=\frac{pM_n}{RT};\ \rho_{\mathrm{cat}}=400\ \mathrm{kg\cdot m^{-3}}$
Viscosity	$\mu_{gas}=\sum_i\frac{1}{1+\frac{1}{x_i}\sum_{j\neq i}x_j\phi_{ij}}$
	$\phi_{ij}=\frac{\left(1+\frac{\mu_i^{0.5}}{\mu_i\mu_j}\cdot\frac{M_i^{0.25}}{M_j}\right)^2}{\frac{4}{\sqrt{2}}\left(1+\frac{M_i}{M_j}\right)^{0.5}}$
Porosity of bed	0.4
Initial porosity of particles	0.3
Initial average aperture	1 nm

3. Results and Discussion

3.1. Model validation

The developed multiscale model was validated against experimental conditions from Ref. [17]. Quantitative agreement was achieved between experimental gas compositions and model predictions, with yield deviations for H_2 (3.2%), CO (4.1%), and CO_2 (2.7%) all below the 5% threshold (Fig. 3(a)). The experimental-simulated comparison of toluene conversion rates over time, as shown in Fig. 3(b), further validating the model's applicability. This validation confirms that the semi-coke-catalyzed reaction kinetic model accurately describes both tar cracking mechanisms and subsequent catalyst deactivation processes.

3.2. Impact of semi-coke catalyst loading on product composition, reactor temperature profile, and pressure distribution

Considering the integral nature of the tar cracking reactor, both the outlet tar concentration and gas processing capacity are influenced by filling volume or height. However, an excessive filling volume can increase the reactor pressure drop and accelerate the tar cracking reaction rate. Therefore, as illustrated in Fig. 4, the impact of semi-coke catalyst loading on product composition, reactor temperature profile, and pressure distribution were evaluated.

As depicted in Fig. 4(a), to achieve a gas product with tar content below 100.00 $mg \cdot m^{-3}$, the reactor requires filling with approximately 108 g of semi-coke catalyst particles. Furthermore, the catalytic reforming of tar significantly enhances the quality of the outlet syngas, increasing the H_2/CO ratio from 0.86 to 1.52. However, when the catalyst charge exceeds 40.00 g in the tar cracking reactor, no statistically significant enhancement in tar removal efficiency is observed, with the purification effect reaching saturation beyond this threshold. As evidenced by Fig. 4(b), the limited improvement in tar removal efficiency can be attributed to the reactor's thermal regime: The system exclusively utilizes intake gas waste heat as its sole thermal source, with complete absence of auxiliary heating. This thermal stratification creates a vertical temperature gradient where upper-bed particles maintain elevated temperatures compared to their lower-bed counterparts. Consequently, diminished reaction kinetics in the cooler upper reactor zone result in suboptimal catalytic performance, thereby diminishing tar treatment capacity. Notably, even when catalyst loading is increased to 40.00 g, thermodynamic equilibrium limitations preclude substantial enhancement in purification efficacy. This phenomenon aligns with Arrhenius kinetics principles, where the 10 °C temperature decrease per 5.00 cm bed height reduction (measured in Fig. 4(b)) corresponds to a 35% to 40% decrease in tar cracking rate constants, as derived from Arrhenius equation simulations. When targeting a semi-coke loading capacity of 108.00 g, as corroborated by Fig. 4(b), axial analysis of the tar cracking reactor reveals progressive intraparticle pore occlusion stemming from coking reactions on the

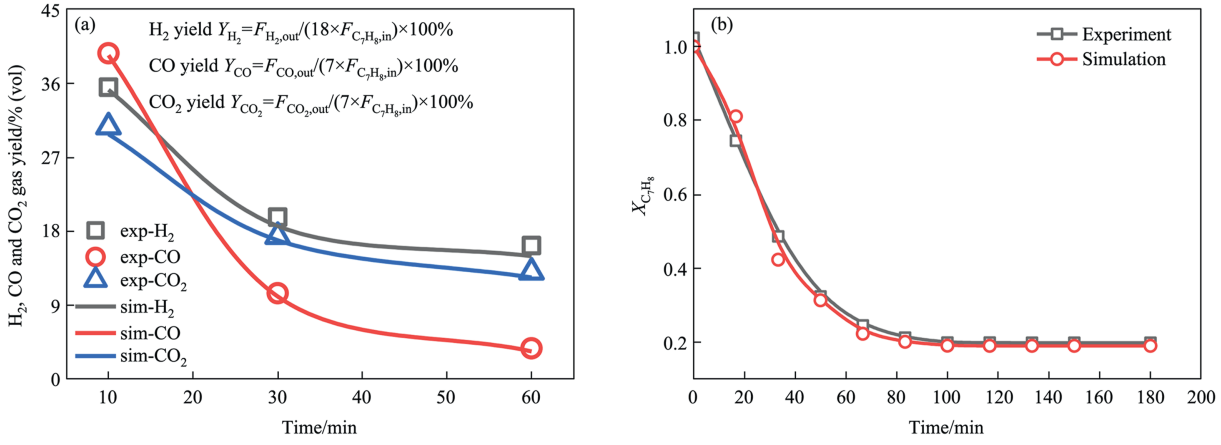

Fig. 3. (a) Verification of catalytic model for semi-coke with product gas yield, (b) the experimental-simulated comparison of toluene conversion rates over time.

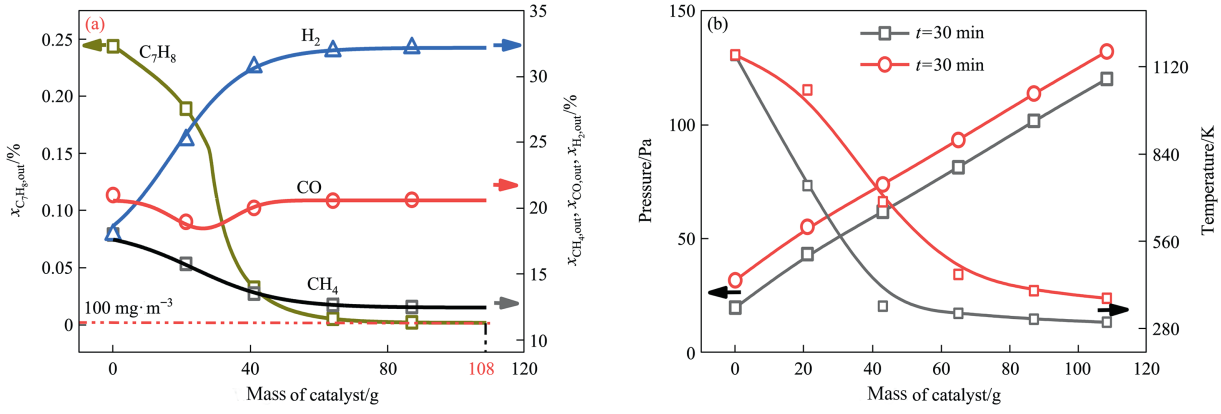

Fig. 4. (a) Impact of semi-coke catalyst loading on product composition, (b) reactor temperature profile, and pressure distribution.

catalyst surface. This structural degradation manifests as a 23% reduction in particle porosity (from 0.58 to 0.45) and a concomitant 150.00 Pa·m^{-1} increase in bed pressure drop along the reactor's longitudinal axis. Notably, bed height escalation beyond 40.00 cm induces exponential growth in pressure differentials, with ΔP surpassing 800.00 Pa at 108 g loading. Such hydrodynamic impairment not only disrupts gas-phase flow uniformity through the packed bed but also compromises syngas purification efficiency by shortening gas-catalyst contact time below 2.3 s (critical threshold for complete tar decomposition).

3.3. Impact of raw syngas inlet temperature on transport-reaction coupling in semi-coke catalyzed tar cracking

The enthalpy flux of raw syngas dictates the thermal boundary conditions for semi-coke-catalyzed cracking reactions, inducing temperature-dependent modulations in both apparent reaction kinetics and catalyst durability profiles. Crucially, thermal gradients across the gas-particle interface modulate interphase heat-mass transport phenomena, as quantitatively mapped in Fig. 5.

Thermal activation of raw syngas (773–1173 K) induces synergistic transport-reaction coupling through carbon-steam gasification thermodynamics ($C + H_2O \rightarrow CO + H_2$, $\Delta G^0 = -32.1$ kJ·mol^{-1} at 1173 K). This endothermic reaction cascade drives a 6.96% enhancement in gas-film heat transfer coefficient (84.45→90.33 W·m^{-2}·K^{-1}) while simultaneously reducing interfacial thermal gradients by 40%. Concurrently, steam-induced pore regeneration elevates semi-coke porosity from 0.38 to 0.51, which synergistically amplifies mass transfer coefficients by 52% (0.017→0.026 m·s^{-1}) and boosts intraparticle effective diffusivity (D_{eff}) from 2.7 × 10^{-6} to 6.3 × 10^{-6} m^2·s^{-1}. These coupled phenomena establish a self-reinforcing mechanism where elevated temperatures suppress carbon deposition while optimizing gas-solid interfacial dynamics. Elevated syngas temperatures (773–1173 K) establish self-reinforcing transport-reaction coupling through dual synergistic mechanisms: (1) Mass transfer intensification driven by steam gasification-induced pore evolution ($\varepsilon = 0.38 \rightarrow 0.51$) enhances gas-solid mass transfer coefficients by 52% (0.017→0.026 m·s^{-1}), reducing boundary layer resistance 38% *via* Sherwood correlation while accelerating species flux through the gas film; (2) Thermal driving force modulation where endothermic carbon-steam reactions ($C + H_2O \rightarrow CO + H_2$, $E_a = 142$ kJ·mol^{-1}) generate intensified Stefan flow, thinning thermal boundary layers to paradoxically boost effective heat transfer coefficients 6.96% (84.45→90.33 W·m^{-2}·K^{-1}) despite 40% reduction in gas-catalyst ΔT (85→51 K). This thermal-activation coupling elevates toluene decomposition kinetics

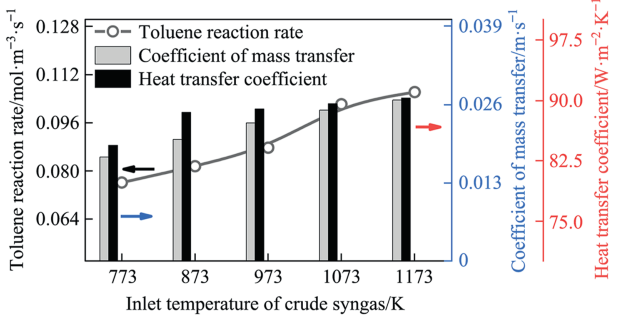

Fig. 5. Thermal activation of raw syngas synergistically enhances gas-solid transport dynamics and toluene decomposition in semi-coke through coupled reaction-transport coupling.

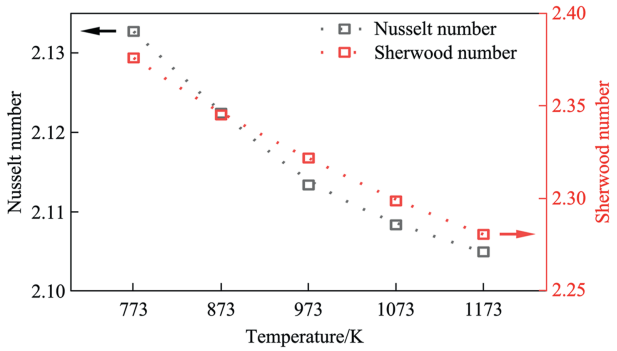

Fig. 6. Impact of raw syngas temperature regulation on heat and mass transfer in semi-coke.

(4.7 × 10^{-5}→8.2 × 10^{-5} mol·(g·s)$^{-1}$) through three synergistic pathways: (i) faster pore diffusion ($D_{eff} = 2.7 \rightarrow 6.3 \times 10^{-6}$ m^2·s^{-1}), (ii) improved catalyst accessibility ($\eta = 0.67 \rightarrow 0.82$), and (iii) 34% suppressed coke formation (0.17→0.11 g coke/g cat per hour). Consequently, tar cracking completeness surges from 78% to >92% at 1173 K, while syngas waste heat recovery efficiency improves from 64% to 79%, demonstrating temperature-mediated optimization of multiphase transport-reaction networks.

The Nusselt number (*Nu*), quantifying the ratio of convective to conductive heat transfer, decreases from 2.13 to 2.10 with rising syngas temperatures (Fig. 6), paradoxically signaling reduced convective dominance despite intensified interfacial heat flux. This stems from competing thermal effects: while elevated gas-solid temperature gradients amplify heat transfer driving forces 32%, concomitant gas-phase property changes—density reduction 18% and viscosity increase 24%—suppress turbulent convection efficiency, as per *Nu* scaling. Conversely, the Sherwood number (*Sh*), representing convective-to-diffusive mass transfer, declines from 2.37 to 2.28 despite enhanced molecular diffusion. Here, thermally activated diffusion elevates gas-film mass transfer coefficients 52%, but the dominance of Fickian diffusion over boundary layer convection reshapes the Sherwood number (*Sh*) balance. Critically, elevated temperatures rebalance transport mechanisms—conductive/diffusive modes gain prominence despite absolute heat/mass flux enhancement, demonstrating thermal optimization of gas-solid transport regimes through viscosity-mediated flow restructuring.

Catalytic deactivation in semi-coke systems arises synergistically from two pathways: (1) carbonaceous deposition *via* tar cracking reactions and (2) reactive consumption of the catalyst matrix by gas-phase intermediates. As evidenced in Fig. 7, thermal

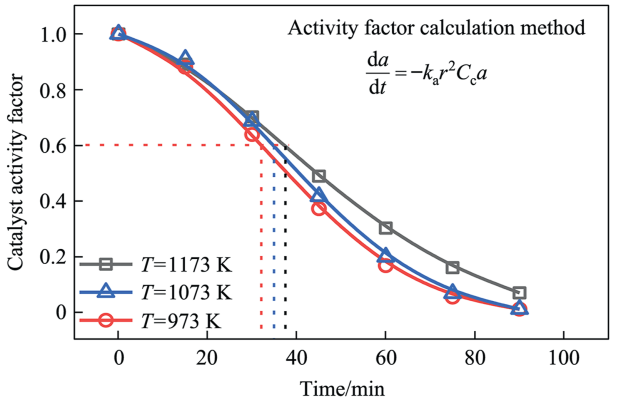

Fig. 7. Impact of raw syngas temperature regulation on semi-coke catalyst activity.

Table 8
The comparison of the catalyst activity factor and porosity before and after the reaction.

Temperature	Catalyst activity factor			Catalyst porosity		
	973 K	1073 K	1173 K	973 K	1073 K	1173 K
Before the reaction	1.00	1.00	1.00	0.30	0.30	0.30
After the reaction (60 min)	0.26	0.28	0.38	0.27	0.25	0.23

regulation of raw syngas composition critically governs activity metrics—elevated temperatures (873–1173 K) paradoxically mitigate deactivation dynamics despite accelerated carbon deposition rates (34% increase), attributed to thermally activated pore restructuring and enhanced coke gasification (CO/CO_2 yield ratio shift from 0.78 to 1.24).

The present study establishes a first-principles deactivation kinetics model through ordinary differential equations (ODEs) that dynamically couple the dimensionless activity coefficient with carbon deposition dynamic, eliminating empirical correlations by directly linking to fundamental carbon accumulation processes rather than time-dependent phenomenological approximations. As quantified in Fig. 7, the semi-coke's catalytic activity undergoes progressive decay during syngas reforming, reaching technical deactivation at 0.6. Thermal modulation from 973 K to 1173 K extends operational lifetime by 18.75% (32→38 min) through two synergistic mechanisms: (1) Tar cracking acceleration, driven by Arrhenius-type enhancement of tar decomposition increases and reduced heavy hydrocarbon polymerization (C/H ratio drops from 1.28 to 0.94); and (2) Steam gasification promotion, evidenced by an elevation in carbon-steam reaction rates and improved pore accessibility. The resultant carbon flux balance—where the deposition rate/Gasification rate ratio decreases from 1.45 to 0.79—preserves critical pore throat diameters (>4.20 nm) and active site availability (>73% metallic sites exposed), thereby stabilizing catalytic functionality through microstructure-optimized thermal regimes.

Due to the deactivation of the catalyst caused by carbon deposits, it is necessary to summarize the physical and chemical properties of the catalyst before and after the reaction, as shown in Table 8.

4. Conclusions

This study establishes a multiscale model for semi-coke catalytic tar removal from raw syngas, integrating intrinsic catalytic activity analysis, dynamic pore structure evolution (driven by carbon deposition/removal), multiphase reaction-transport coupling mechanisms (distinguishing homogeneous/heterogeneous reaction pathways), and gas-solid non-isothermal heat transfer (maximum temperature difference ~58 K). The framework achieves multiscale simulations spanning reactor hydrodynamics (Re = 1200–4500) to catalyst particle microstructure evolution (pore size: 4.20–18.70 nm). The model reveals the correlation mechanism between the carbon deposition-gasification dynamic equilibrium (rate ratio: 0.79–1.45) and microstructural destabilization thresholds of catalysts. It provides a quantitative predictive tool for the design optimization of consumable matrix catalytic systems, demonstrating particular application value in predicting catalyst lifespan and regulating pore evolution pathways.

CRediT authorship contribution statement

Jie Feng: Writing – review & editing, Supervision, Methodology, Funding acquisition, Conceptualization. Jun Xue: Writing – original draft, Methodology, Investigation, Data curation. Yaowei Hu: Validation. Yuncai Song: Writing – review & editing, Validation, Funding acquisition, Conceptualization. Wenying Li: Writing – review & editing, Resources, Funding acquisition.

Declaration of Competing Interest

The authors declare that they have no known competing financial interests or personal relationships that could have appeared to influence the work reported in this paper.

Acknowledgements

This work was financially by the National Key Research and Development Program of China (2022YFE0208400), the Shanxi Province Key Research and Development Program (202202090301002), and the Natural Science Foundation of Shanxi Province, China (202103021224096).

Nomenclature

C_p	specific heat capacity at constant pressure, $J\cdot kg^{-1}\cdot K^{-1}$
$D_{eff,i}$	the effective diffusion coefficient of component i, $m^2\cdot s^{-1}$
F	volume force vector, $N\cdot m^{-3}$
$h_{pe,f}$	the heat transfer coefficient of the particle surface, $W\cdot m^{-2}\cdot K^{-1}$
I	matrix of identity
j_i	the mass flux of substance i, $kg\cdot m^{-2}$
k_{pe}	particle permeability, m^{-2}
M_i	the molar mass of substance i, $g\cdot mol^{-1}$
M_n	mean molar mass of the pooled components, $g\cdot mol^{-1}$
P	pressure, Pa
q	heat flux, $W\cdot m^{-2}$
Q	reaction heat source term, $W\cdot m^{-3}$
Q_m	mass source term, $kg\cdot s^{-1}$
R_i	the reaction rate of substance i, $kg\cdot m^{-3}\cdot s^{-1}$
T	absolute temperature, K
u	velocity of fluid, $m\cdot s^{-1}$
u_r	the percolation velocity within the particle, $m\cdot s^{-1}$
w_i	the mass fraction of substance i
X_i	conversion of i
x_c	biochar conversion rate
x_i	molar fraction of i
ε_p	porosity of the bed
ε_{pe}	porosity of semi-coke particles
ρ	density of fluid, $kg\cdot m^{-3}$
ψ	particle structure parameter

References

[1] D. Xu, Y.Q. Xiong, J.D. Ye, Y.H. Su, Q. Dong, S.P. Zhang, Performances of syngas production and deposited coke regulation during co-gasification of biomass and plastic wastes over Ni/γ-Al_2O_3 catalyst: role of biomass to plastic ratio in feedstock, *Chem. Eng. J.* 392 (2020) 123728.
[2] X. Zeng, F. Wang, H.L. Li, Y. Wang, L. Dong, J. Yu, G.W. Xu, Pilot verification of a low-tar two-stage coal gasification process with a fluidized bed pyrolyzer and fixed bed gasifier, *Appl. Energy* 115 (2014) 9–16.

[3] Y.F. Shen, Chars as carbonaceous adsorbents/catalysts for tar elimination during biomass pyrolysis or gasification, *Renew. Sustain. Energy Rev.* 43 (2015) 281−295.
[4] V. Ahuja, A.K. Palai, A. Kumar, A.K. Patel, A.A. Farooque, Y.H. Yang, S.K. Bhatia, Biochar: empowering the future of energy production and storage, *J. Anal. Appl. Pyrolysis* 177 (2024) 106370.
[5] R. Potnuri, D.V. Surya, C.S. Rao, A. Yadav, V. Sridevi, N. Remya, A review on analysis of biochar produced from microwave-assisted pyrolysis of agricultural waste biomass, *J. Anal. Appl. Pyrolysis* 173 (2023) 106094.
[6] C. Di Stasi, S. Renda, G. Greco, B. González, V. Palma, J.J. Manyà, Wheat-straw-derived activated biochar as a renewable support of Ni-CeO_2 catalysts for CO_2 methanation, *Sustainability* 13 (16) (2021) 8939.
[7] Z. Abu El-Rub, E.A. Bramer, G. Brem, Experimental comparison of biomass chars with other catalysts for tar reduction, *Fuel* 87 (10−11) (2008) 2243−2252.
[8] M. Zhang, G.F. Fan, N. Liu, M.D. Yang, X.X. Li, Y.L. Wu, Tar removal in pine pyrolysis catalyzed by bio-char supported nickel catalyst, *J. Anal. Appl. Pyrolysis* 169 (2023) 105843.
[9] W.Q. Fan, M.H. Tahir, D.Z. Chen, L. Hong, L.J. Yin, H.M. Yu, High quality oil and H_2-rich gas production from municipal solid wastes through pyrolysis and catalytic reforming: Comparison of differently modified waste char-based catalysts, *J. Anal. Appl. Pyrolysis* 178 (2024) 106382.
[10] H.L. Sun, D.D. Feng, Y.J. Zhao, S.Z. Sun, J.Q. Wu, P.X. Wang, G.Z. Chang, X.Y. Lai, H.P. Tan, Y.K. Qin, Mechanism of catalytic tar reforming over biochar: description of volatile-H_2O-char interaction, *Fuel* 275 (2020) 117954.
[11] N. Wang, D.Z. Chen, U. Arena, P.J. He, Hot char-catalytic reforming of volatiles from MSW pyrolysis, *Appl. Energy* 191 (2017) 111−124.
[12] C.Y. Deng, W.J. Song, Z. Chai, S. Guo, Z.P. Zhu, Characteristics of tar thermal cracking and catalytic conversion during circulating fluidized bed char gasification, *Energy Fuel.* 34 (1) (2020) 142−149.
[13] X. Zeng, F. Wang, Z.N. Han, J.Z. Han, J.L. Zhang, R.C. Wu, G.W. Xu, Assessment of char property on tar catalytic reforming in a fluidized bed reactor for adopting a two-stage gasification process, *Appl. Energy* 248 (2019) 115−125.
[14] N. Muradov, F. Smith, A. T-Raissi, Catalytic activity of carbons for methane decomposition reaction, *Catal. Today* 102-103 (2005) 225−233.
[15] A. Voorhies Jr., Carbon formation in catalytic cracking, *Ind. Eng. Chem.* 37 (4) (1945) 318−322.
[16] D. Buentello-Montoya, X.L. Zhang, J. Li, V. Ranade, S. Marques, M. Geron, Performance of biochar as a catalyst for tar steam reforming: effect of the porous structure, *Appl. Energy* 259 (2020) 114176.
[17] Y. Song, Y. Chen, Y. Song, J. Feng, Catalyst design and reactor analysis for *in-situ* purification of organic solid waste syngas, *Chem. Ind. Eng. Prog.* 42 (2023) 1383−1396. (in Chinese)
[18] J.T. Richardson, S.A. Paripatyadar, Carbon dioxide reforming of methane with supported rhodium, *Appl. Catal.* 61 (1) (1990) 293−309.
[19] J.W. Snoeck, G.F. Froment, M. Fowles, Filamentous carbon formation and gasification: thermodynamics, driving force, nucleation, and steady-state growth, *J. Catal.* 169 (1) (1997) 240−249.
[20] Y. Song, J. Feng, W. Li, A reaction device for catalytic cracking of tar with a carbon-based catalyst, US Pat., CN214881318U (2021). (in Chinese)
[21] J.J. Carberry, A boundary-layer model of fluid-particle mass transfer in fixed beds, *AIChE J.* 6 (3) (1960) 460−463.
[22] N. Kishore, S. Gu, Momentum and heat transfer phenomena of spheroid particles at moderate Reynolds and Prandtl numbers, *Int. J. Heat Mass Tran.* 54 (11−12) (2011) 2595−2601.
[23] F. Yoshida, D. Ramaswami, O.A. Hougen, Temperatures and partial pressures at the surfaces of catalyst particles, *AIChE J.* 8 (1) (1962) 5−11.
[24] D.J. Gunn, Transfer of heat or mass to particles in fixed and fluidised beds, *Int. J. Heat Mass Tran.* 21 (4) (1978) 467−476.
[25] J.W. Snoeck, G.F. Froment, M. Fowles, Steam/CO_2 reforming of methane. carbon filament formation by the Boudouard reaction and gasification by CO_2, by H_2, and by steam: kinetic study, *Ind. Eng. Chem. Res.* 41 (17) (2002) 4252−4265.
[26] U. Oemar, M.L. Ang, K. Hidajat, S. Kawi, Mechanism and kinetic modeling for steam reforming of toluene on $La_{0.8}Sr_{0.2}Ni_{0.8}Fe_{0.2}O_3$ catalyst, *AIChE J.* 60 (12) (2014) 4190−4198.
[27] S.G. Zavarukhin, G.G. Kuvshinov, The kinetic model of formation of nanofibrous carbon from CH_4−H_2 mixture over a high-loaded nickel catalyst with consideration for the catalyst deactivation, *Appl. Catal. Gen.* 272 (1−2) (2004) 219−227.
[28] X. Zeng, L.M. Wang, F. Wang, D.D. Hu, P. Wu, X.Y. Lai, Comparison of reaction characteristics and kinetics between tar thermal cracking and steam reforming in a micro fluidized bed reaction analyzer, *J. Anal. Appl. Pyrolysis* 169 (2023) 105846.
[29] J. Fermoso, M.V. Gil, C. Pevida, J.J. Pis, F. Rubiera, Kinetic models comparison for non-isothermal steam gasification of coal−biomass blend chars, *Chem. Eng. J.* 161 (1−2) (2010) 276−284.
[30] M.M. Sun, J.L. Zhang, K.J. Li, K. Guo, Z.M. Wang, C.H. Jiang, Gasification kinetics of bulk coke in the CO_2/CO/H_2/H_2O/N_2 system simulating the atmosphere in the industrial blast furnace, *Int. J. Miner. Metall. Mater.* 26 (10) (2019) 1247−1257.
[31] M. Yan, M. Zeng, Q.Y. Chen, Q.W. Wang, Numerical study on carbon deposition of SOFC with unsteady state variation of porosity, *Appl. Energy* 97 (2012) 754−762.